iScience

CellPress
OPEN ACCESS

Article

EEG error-related potentials encode magnitude of errors and individual perceptual thresholds

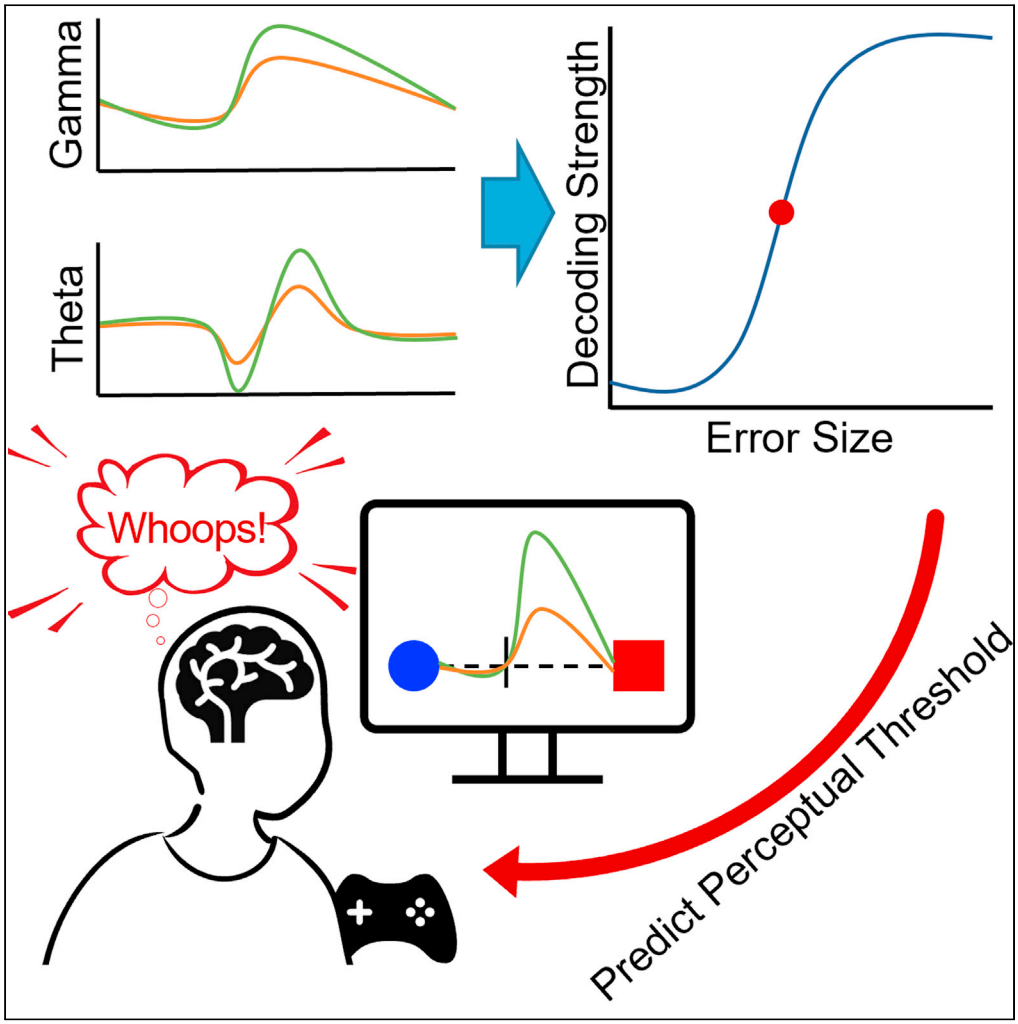

Fumiaki Iwane, Aleksander Sobolewski, Ricardo Chavarriaga, José del R. Millán

jose.millan@austin.utexas.edu

Highlights

BCI continuously monitored presence of ErrPs in real-time

ErrPs encode magnitude of errors and individual perceptual ability

ErrP decoder transfers across sessions and scales over varying magnitude of errors

Theta-gamma brain oscillatory coupling predicted amount of motor adaptation

Iwane et al., iScience 26, 107524
September 15, 2023
https://doi.org/10.1016/j.isci.2023.107524

iScience

CellPress
OPEN ACCESS

Article

EEG error-related potentials encode magnitude of errors and individual perceptual thresholds

Fumiaki Iwane,[1,2,3] Aleksander Sobolewski,[4,5] Ricardo Chavarriaga,[5,6] and José del R. Millán[1,2,5,7,8,*]

SUMMARY

Error-related potentials (ErrPs) are a prominent electroencephalogram (EEG) correlate of performance monitoring, and so crucial for learning and adapting our behavior. It is poorly understood whether ErrPs encode further information beyond error awareness. We report an experiment with sixteen participants over three sessions in which occasional visual rotations of varying magnitude occurred during a cursor reaching task. We designed a brain-computer interface (BCI) to detect ErrPs that provided real-time feedback. The individual ErrP-BCI decoders exhibited good transfer across sessions and scalability over the magnitude of errors. A non-linear relationship between the ErrP-BCI output and the magnitude of errors predicts individual perceptual thresholds to detect errors. We also reveal theta-gamma oscillatory coupling that co-varied with the magnitude of the required adjustment. Our findings open new avenues to probe and extend current theories of performance monitoring by incorporating continuous human interaction tasks and analysis of the ErrP complex rather than individual peaks.

INTRODUCTION

Skillful tennis players can hit and return a ball with the desired effect because of their ability to identify errors between the predicted next states and the actual ones along the trajectory, which enables them to adjust their actions seamlessly.[1] However, this is a challenging task for novice players. This individual variability in our ability to detect errors of varying degrees is key for sensorimotor and adaptation learning.[2,3] While previous research has uncovered a neural correlate of performance monitoring in the human electroencephalogram (EEG) elicited by the awareness of discrete erroneous actions, the so-called error-related potentials (ErrPs),[4–8] little is known about whether these potentials encode the magnitude of errors. Some previous studies have reported co-varying characteristics of the ErrP with error magnitudes[9–13] –such as amplitude or phase coherence–, while others did not.[14] Although previous studies suggested a linear relationship between the magnitude of errors and amplitude of ErrPs,[9,10] a major limitation of these studies is the use of a limited number of error categories (i.e., small, medium, and large) that failed to capture a continuous relationship between the magnitude of errors and the characteristics of the ErrP. Such a relationship is critical to predict our individual ability to discern errors.

Here, we designed an experiment to further investigate these two open questions –namely, does ErrP encode the magnitude of errors? Can they predict the individual threshold of error awareness?–, where occasional visual rotations occur during a cursor reaching task. We also developed a brain-computer interface (BCI) to detect in real time the presence or absence of an ErrP in the subjects' EEG indicating a rotation of the joystick-to-cursor mapping. Critically, in our study, induced errors are not constant, so as to avoid any adaptation process, and are variable in magnitude.

ErrPs are elicited when subjects perceive an erroneous action, either committed by themselves[4,5] or by another person or agent.[7,15] The ErrP is characterized by two main deflections thought to be originated mainly from the anterior cingulate cortex (ACC),[6,16–19] an initial error-related negativity (ERN) followed by a positive peak (Pe), observed over the frontocentral cortex. Further, a recent study found an increase of high-gamma band power along with ErrPs.[20] Nevertheless, reports on the co-activating high-gamma activity are still limited and required further examination.

ErrP-BCIs have shown to enable seamless and intuitive interaction with external devices.[8,15,21–26] Nevertheless, in these studies actions were executed at discrete steps, not continuously as required here. Some BCIs

[1]Department of Electrical and Computer Engineering, The University of Texas at Austin, Austin, TX 78712, USA

[2]Department of Neurology, The University of Texas at Austin, Austin, TX 78712, USA

[3]Learning Algorithms and Systems Laboratory (LASA), École Polytechnique Fédérale de Lausanne (EPFL), 1015 Lausanne, Switzerland

[4]Wyss Center for Bio and Neuroengineering, Campus Biotech, 1202 Genève, Switzerland

[5]École Polytechnique Fédérale de Lausanne (EPFL), Campus Biotech, 1202 Genève, Switzerland

[6]Centre for Artificial Intelligence, Zurich University of Applied Sciences (ZHAW), 8401 Winterthur, Switzerland

[7]Mulva Clinic for the Neurosciences, The University of Texas at Austin, Austin, TX 78712, USA

[8]Lead contact

*Correspondence: jose.millan@austin.utexas.edu

https://doi.org/10.1016/j.isci.2023.107524

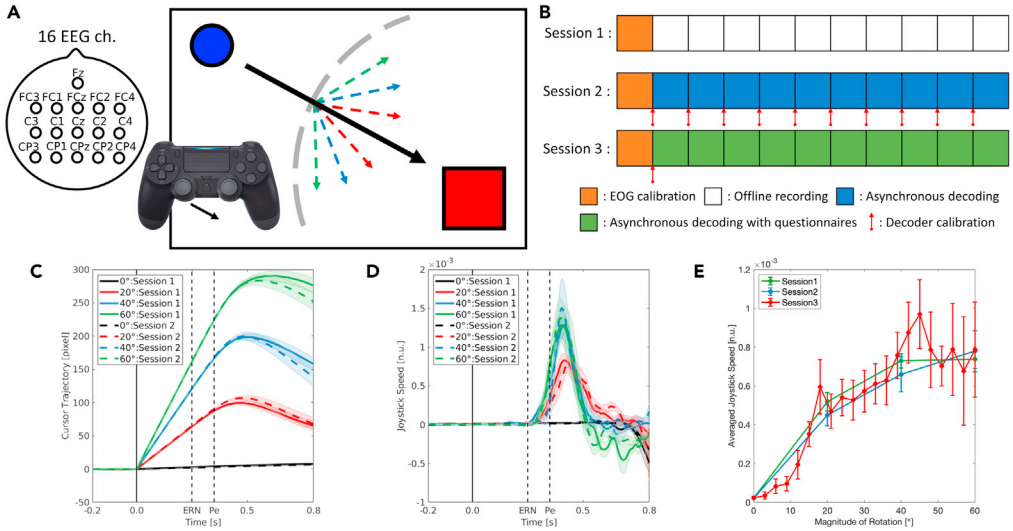

Figure 1. Overview of the experimental protocol and behavioral results

(A) Graphical representation of the experimental design. The blue circle indicates a cursor controlled by the left-joystick of a game-pad. The red square represents the goal location where participants were instructed to bring the cursor as quickly as possible. Black arrow indicates the optimal cursor trajectory (straight line) to the goal. Gray dashed line represents the boundary to induce visual rotations, which was randomly defined for each trial. In a correct trial (70% of trials), no visual rotation occurred. In error trials (30%) of sessions 1 and 2, visual rotations could be 20° (red), 40° (blue) or 60° (green), while in session 3 rotations were from 3° to 60° with a step of 3° (lines not shown). All lines were invisible to participants during the experiment. Note that participants cannot predict occurrence of visual rotations nor their magnitude.

(B) Experimental timeline for each recording session. 90 s of EOG calibration data were recorded before the cursor reaching task. In session 1, participants underwent the experiment without BCI feedback. In session 2, presence of ErrPs was continuously monitored while updating the decoder after each run. In session 3, continuous decoding was performed with a fixed decoder.

(C and D) Cursor deviations from straight trajectories and joystick speed in sessions 1 and 2 (mean, continuous or dotted lines, and SE, shaded areas).

(E) Joystick speed of all sessions within the time window of [0.35, 0.45] s (mean ± SE).

See also Figures S1 and S4.

have succeeded in decoding the presence of an ErrP during a continuous task.[27–30] However, these studies used experimental protocols where erroneous actions are abrupt stops of the device,[27,28] errors happen at the same moment during the interaction,[29,31] or the device fails to reach a target[30]—all extreme conditions that do not capture erroneous actions during a continuous interaction, but see Batzianoulis et al.[32] Furthermore, none of these previous studies characterized the ErrPs as a function of the severity of the erroneous action.

We designed a BCI experiment consisting of three recording sessions, in which ErrPs were elicited by a visual rotation while the subject was using a joystick to continuously control a computer cursor to reach a target (Figures 1A and 1B; Table 1 and Video S1). Errors (rotations of the joystick-to-cursor mapping) were induced in 30% of the trials. On the first and second recording sessions, subjects performed the cursor reaching task with three different degrees of rotation; i.e., 20°, 40° and 60°. On the third session, subjects experienced a finer range of rotations; i.e., from 3° to 60° with a step of 3°, to characterize the ErrP over the continuous magnitude of errors. Furthermore, online continuous decoding of ErrPs were performed on the second and the third sessions in a "Plug-and-Play" manner[33] by using the data from the previous recording session. The BCI provided real-time feedback to participants by changing the color of the cursor upon ErrP detection.

RESULTS

Consistent behavior over the three experimental sessions

Participants generated similar cursor trajectories across recording sessions and consistently initiated corrective actions at 0.3 s with respect to the onset of the rotation (Figures 1C and 1D). The peak joystick

Table 1. Time differences in days between the three recording sessions

Subject ID	s1	s2	s3	s4	s5	s6	s7	s8	s9	s10	s11	s12	s13	s14	s15	s16	mean ± SE
Session1 - Session2	52	63	42	42	51	49	56	56	51	59	43	44	35	24	35	37	46 ± 3
Session2 - Session3	25	13	40	35	38	38	28	31	26	11	32	45	52	32	21	10	30 ± 3

speed was observed at 0.41, 0.40, and 0.42 s for the first, second, and third session, respectively. The mean joystick speed increased along magnitude of rotation while keeping consistency over the recording sessions (Figure 1E). Variance of averaged joystick speed was larger on the third session compared with the first and the second session due to the lower number of trials recorded for each magnitude of rotation (n = 6 ± 1 [mean ± SD]). We also measured their levels of engagement for the duration of the experiment based on the reaction time between the onset of a trial and the initiation of cursor control. The average level of engagement remained consistent throughout the ten runs of the experiment (Figure S1A). Altogether, participants had a uniform behavior over the three recording sessions, and the speed of joystick movement was a function of the magnitude of errors.

It is possible that participants make erroneous corrective actions in our experiments. To calculate the number of erroneous corrective actions, we measured the distance between the cursor and the goal within the 1 s time window following the onset of rotation. Since the visual rotations ranged from −60 to 60°, the distance decreased even without corrective actions. The distance increased only when participants misdelivered their corrective actions. Erroneous corrective actions were observed in only 3.9 ± 0.7% (mean ± SE) of the trials with visual rotations.

Theta-gamma brain oscillatory coupling co-varies with magnitude of errors

We observed band specific power modulation for theta [4, 8] Hz,[29,30] beta [18, 30] Hz[34,35] and gamma [60, 90] Hz rhythms[20] (Figures 2A and 2B). Theta band exhibited increased power modulation within the time window of [0.1, 0.6] s with respect to the onset of rotation. Beta and gamma band showed simultaneous modulations within the time window of [0.3, 0.8] s. While beta band power decreased, gamma band power increased when participants observed and corrected a visual rotation (paired Wilcoxon signed-rank test, $p < 0.001$ for all three frequency bands). Whereas the two conditions of the control experiment (Figure S4), active and playback, also induced modulations of theta power as a function of the degree of visual rotation, the decreased beta and increased gamma activity after visual rotations were not observed in neither of the conditions of the control study (Figures S5 and S6).

Theta and gamma band activity were modulated by the magnitude of rotation, while beta band activity remained stable for the varying magnitudes of rotation (Figure 2C). Furthermore, at ERN, we observed phase-amplitude coupling between high theta ([6, 8] Hz) and gamma band, while at Pe, coupling occurred between low theta ([4, 6] Hz) and gamma band (Figure 2D). Similar to the temporal band power, phase-amplitude coupling increased for larger magnitudes of rotation. These results confirm that theta and gamma band activity, as well as their interaction, encode the magnitude of errors, while this is not the case for beta band activity.

ErrP-BCI decoder exhibits transferability and scalability

The amplitude of ErrPs increased and the latency of the deflections shortened as the magnitude of rotations increased (Figures 3A and 3B). We also observed this relationship in the control experiment for both conditions, active and playback (Figure S5).

In the third session (Figure 3C) it is observed the two prominent deflections in the ErrPs when participants consciously perceived the rotation (*Yes*), and similar but delayed and smaller sequential peaks when participants were not sure whether they observed the rotation (*Maybe*). Topographical representations of all trials with rotation (insets in Figures 3A–C) show similar patterns in the three recording sessions; namely, broad activation of the central area at 0.25 s, followed by focal activation of the fronto-central area at 0.35 s. An activation of the parieto-central area was also observed at 0.4 s relative to onset of errors (Figure S2). The observed topographies are consistent with previous studies,[36,37] where errors are not self-generated. These results suggest that ErrPs encode magnitude of errors in its amplitude and latency and are stable across different recording sessions.

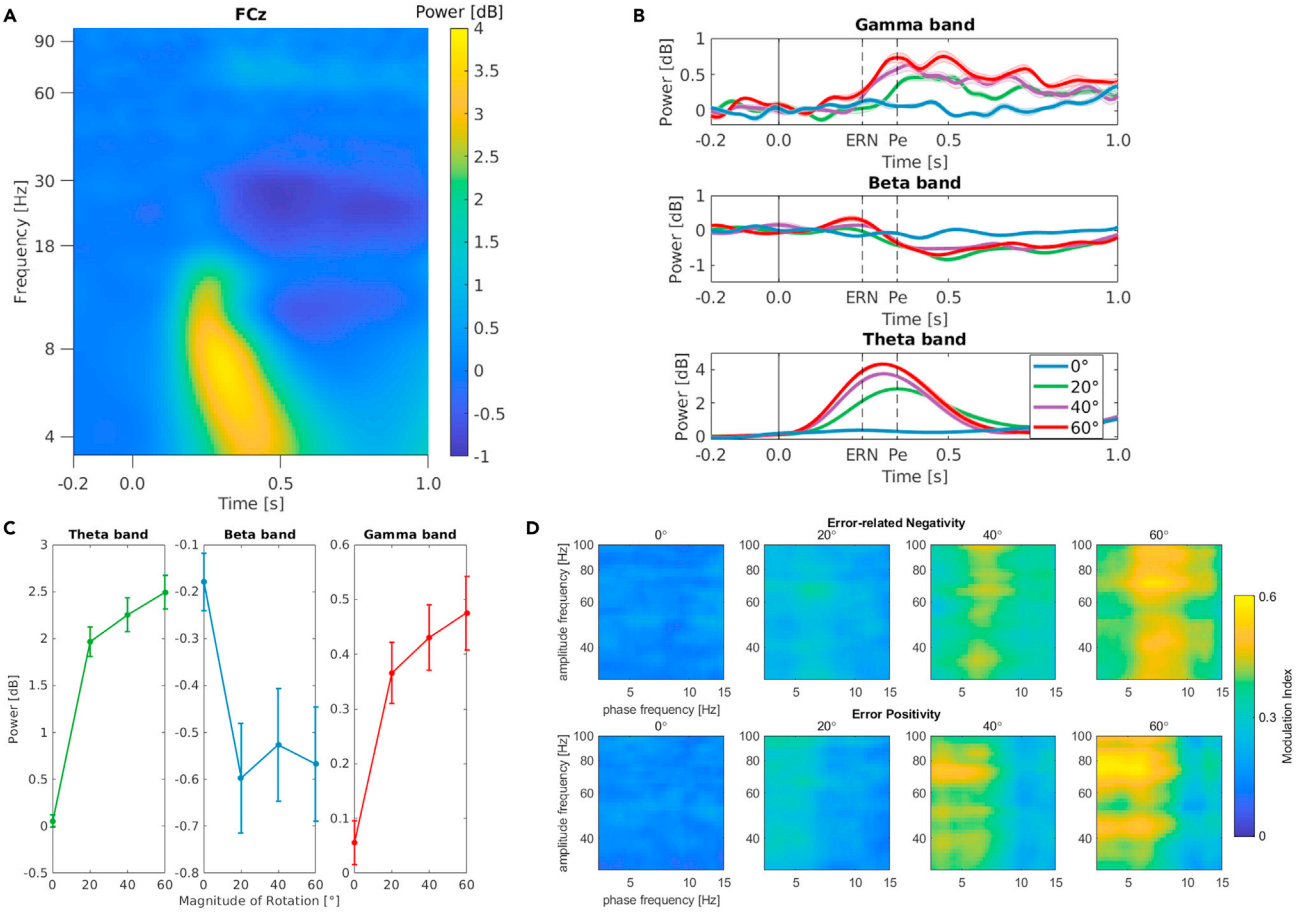

Figure 2. Time-frequency representations of ErrPs at FCz electrode on the first two sessions

(A) Time-frequency decomposition of ErrPs averaged over all rotation trials with respect to the onset of rotation. Power was normalized by pre-stimuli baseline ([-0.25, 0.0] s).

(B) Theta (4–8 Hz), beta (18–30 Hz) and gamma band (60–90 Hz) power modulation with respect to the onset of event (x = 0 s) for each magnitude of rotation (mean ± SE). Two dashed black lines at 0.25 s and 0.35 s indicate when ERN and Pe appeared. Theta band power increased within the time window of [0.1, 0.6] s with respect to the onset of rotation. Beta band power decreased, while gamma band power showed increase within the time window of [0.3, 0.8] s.

(C) Averaged band power modulation for each magnitude of rotation of the first two sessions (mean ± SE). Theta and gamma band power in erroneous trials were modulated as a function of magnitude of rotation (Spearman's correlation analysis, Theta: $r = 0.70$, $p < 0.001$, Gamma: $r = 0.39$, $p < 0.001$), while beta band activity remained stable for the different magnitudes of rotation (Spearman's $r = 0.10$, $p = 0.33$).

(D) Theta-gamma phase-amplitude coupling at ERN and Pe. Coupling is larger for trials with larger magnitude of rotations.

See also Figure S6.

Decoding performance was similar across sessions (for different rotations in the first two sessions, and balanced accuracy in the third sessions, Figures 3D and 3E; Table 2). TPR increased along with the magnitude of rotation in all conditions of classification (time-locked classification of the first and the second session and continuous classification of the second session, Figure 3D). The continuous classification performance (balanced accuracy) was significantly lower than the time-locked classification in the second and third sessions (paired Wilcoxon signed-rank test, $p < 0.001$ for both sessions), which illustrates the challenge to perform continuous decoding of ErrPs.

During continuous decoding, presence of ErrPs were consistently detected with high temporal accuracy at around 0.85 s after the onset of rotation (Figure 3F), which corresponds to the time window used to train the classifier, [0.2, 0.8] s (second session: 0.853 ± 0.01 s, third session: 0.846 ± 0.01 s). Run-wise recalibration of the decoder increased continuous decoding performance over the ten runs on the second session (Figure S3). We then characterized the continuous relationship between the magnitude of rotations and the BCI output over the three sessions (Figure 4). Estimated posterior probabilities of time-locked classification

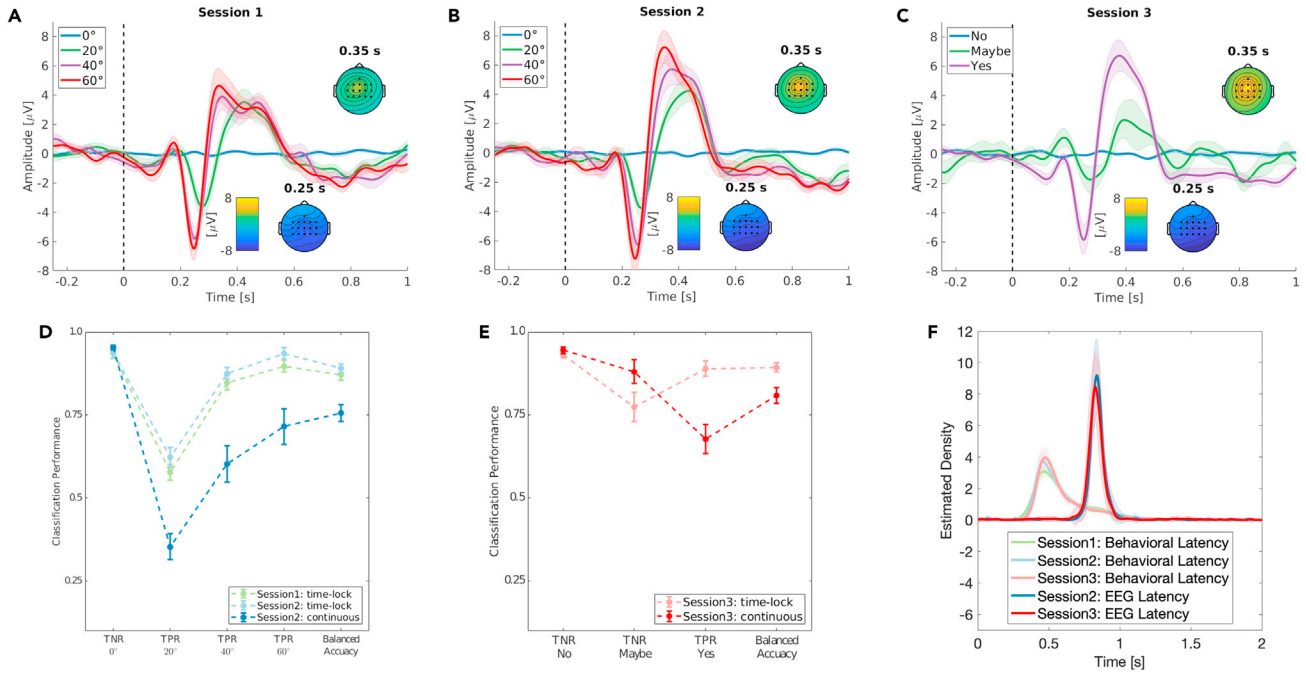

Figure 3. Grand-averaged signals and classification performance

(A–C) Grand-averaged signals at FCz channel for each recording session, respectively (mean ± SE). The dashed line (x = 0 s) represents the onset of rotation. On the first two sessions, each line corresponds to a magnitude of rotation; while lines correspond to the subjective behavioral answers on the third session (mean; continuous lines, and standard error; shaded areas). Each panel includes topographical representations averaged over trials with rotation of the negative and positive deflections at 0.25 and 0.35 s.

(D and E) Classification performance for time-locked classification and continuous decoding on the first two sessions and the third session, respectively (mean ± SE). Note that True positive rate (TPR) increased as a function of magnitude on session 1 and 2.

(F) Latency of the behavioral correction and online continuous decoding with respect to the onset of rotations (x = 0 s, mean ± SE). Light colored lines correspond to the onset of the corrective movement for the three sessions while dark colored lines represent latency to detect ErrPs on session 2 and 3. See also Figures S2, S3, and S5.

ranged from 0.21 (0°) to 0.78 on the first two sessions and to 0.86 on the third session (60°), while it ranged from 0.63 to 0.93 on the second and third sessions for continuous classification. For both, time-locked and continuous decoding, the estimated posterior probability linearly increased until 30°, then plateaued for larger rotations. Thus, an exponential model successfully captured the modulation over the magnitudes of visual rotation. These results illustrate that the ErrP-BCI output encodes not only errors, but also their magnitude.

ErrP-BCI output predicts individual perceptual thresholds

Finally, we asked whether ErrPs predict individual perceptual thresholds to detect visual rotations. To answer this question, we analyzed the ErrP-BCI output in the time-locked condition of the third session. The perceptual threshold is defined as the magnitude of rotation for which participants detected only 50% of occurrences. On average, participants started to answer "Maybe" at 8 ± 3° and "Yes" at 12 ± 5 degrees of rotation (Figure 5A). Most importantly, the behavioral answer and the output of the ErrP-BCI were modulated similarly, demonstrating the transferability of the decoder over sessions and the scalability of ErrPs over the different magnitudes of rotation. The inferred individual perceptual threshold from the ErrP-BCI predicted the behavioral individual perceptual threshold (Spearman's r = 0.60, p = 0.015, Figure 5B), while having comparable median values (paired Wilcoxon signed-rank test, p = 0.96). We further verified that the levels of engagement of the third session (time duration between the onset of trials and initiation of cursor movement) did not explain the individual perceptual threshold (Spearman's r = 0.18, p = 0.51, Figure S1B). In summary, individual ability to detect errors was successfully inferred by characterizing the relationship between the magnitude of errors and their corresponding ErrPs.

Table 2. Time-locked classification and online continuous decoding performance for each recording session (mean ± SE)

Time-locked classification						
Training session	Test session	TNR of 0°	TPR of 20°	TPR of 40°	TPR of 60°	Balanced Accuracy
Session 1	Session 1	93.63 ± 1.54	57.73 ± 2.31	84.76 ± 2.13	89.74 ± 1.77	87.13 ± 1.65
Session 1	Session 2	93.84 ± 1.66	62.27 ± 2.88	87.55 ± 1.78	93.59 ± 1.77	89.16 ± 1.29
Training session	Test session	TNR of *No*	TNR of *Maybe*	TPR of *Yes*		Balanced Accuracy
Session 1 and 2	Session 3	93.13 ± 0.97	77.52 ± 4.38	89.99 ± 2.32		89.38 ± 1.38
Continuous decoding						
Training session	Test session	TNR of 0°	TPR of 20°	TPR of 40°	TPR of 60°	Balanced Accuracy
Session 1	Session 2	95.30 ± 0.76	35.37 ± 3.86	60.37 ± 5.48	71.54 ± 5.34	75.64 ± 2.51
Training session	Test session	TNR of *No*	TNR of *Maybe*	TPR of *Yes*		Balanced Accuracy
Session 1 and 2	Session 3	94.54 ± 0.97	88.11 ± 3.52	67.84 ± 4.38		80.96 ± 2.36

Balanced accuracy was computed by using data with all magnitude of errors.

DISCUSSION

Our results indicate that ErrPs encode not only the conscious perception of errors (i.e., visual rotations in our experimental setup) (Figure 3C), but also their magnitude, in their amplitude and latency (Figures 3A and 3B). Furthermore, classification results from session 3 demonstrates how the ErrP decoder —built from data of sessions 1 and 2 that contains only rotations of 0°, 20°, 40° or 60°— generalizes across rotations ranging from 0° to 60° with a step of 3° and across recording sessions (Figure 4). More fundamentally, analysis of the ErrP-BCI output shows that ErrPs predict individual perceptual thresholds to detect a visual rotation.

In the present study, participants used a joystick to control a cursor to reach a target (Figure 1A). Unlike typical visual rotation tasks,[13,38–40] the visual coupling between the cursor movement and the joystick was occasionally disrupted during the continuous cursor controlling task with varying magnitudes to ensure participants could predict cursor trajectories and, so, elicit ErrPs in their EEG. This design enabled to induce stable and precise perturbations on the cursor trajectory and associated corrective actions across sessions (Figures 1C and 1D). Furthermore, the elicited ErrPs were also stable across the three recording sessions (Figure 3), in line with previous findings.[8,21,41] On average, 46 and 30 days elapsed between consecutive sessions, respectively (Table 1).

While most theories of performance monitoring consider ErrPs as a detector,[36,42] some studies report that amplitude of ErrPs co-vary with the magnitude of errors.[9–13] In those studies, amplitude of Pe[11] or both ERN and Pe[13] co-varied with the magnitude of errors induced by visual rotations. A consistent relationship was identified for ERN with kinematic errors,[12] for both ERN and Pe with pointing error[10] and observational errors in a virtual reality setup.[9] Previous studies thus proposed a linear relationship between the magnitude of errors and ErrPs.[9,10] However, the magnitude of errors was limited to a short number of discrete error categories (i.e., small, medium, and large), thus not capturing a continuous relationship between the two —which is crucial to explain our individual ability to detect errors. Moreover, whether or not ErrPs encode magnitudes of errors has remained controversial. Another study reported that different magnitudes of a visual rotation do not affect ErrPs by comparing rotations of 45° and 180°.[14] Our results extend and reconcile previous research as we have identified a continuous non-linear relationship between the magnitude of errors and the output of the ErrP-BCI, which starts plateauing after 30° of rotation (Figure 4). The observed relationship remained consistent in the control experiment for both conditions, active and playback (Figure S5).

Having established this non-linear relationship, one fundamental question arises; namely, "Can we infer participants' perceptual threshold to detect errors?". Behavioral answers to conscious perception of errors and inferred subjects' responses from ErrPs were similarly modulated along with the magnitude of rotation (Figure 5A). Interestingly, we observed that even at the magnitude where participants were unsure about the presence of the rotation (i.e., "Maybe") the behavioral and inferred answers were closely aligned to each other. ErrPs for "Maybe" exhibited smaller and delayed deflections than for ErrPs elicited by

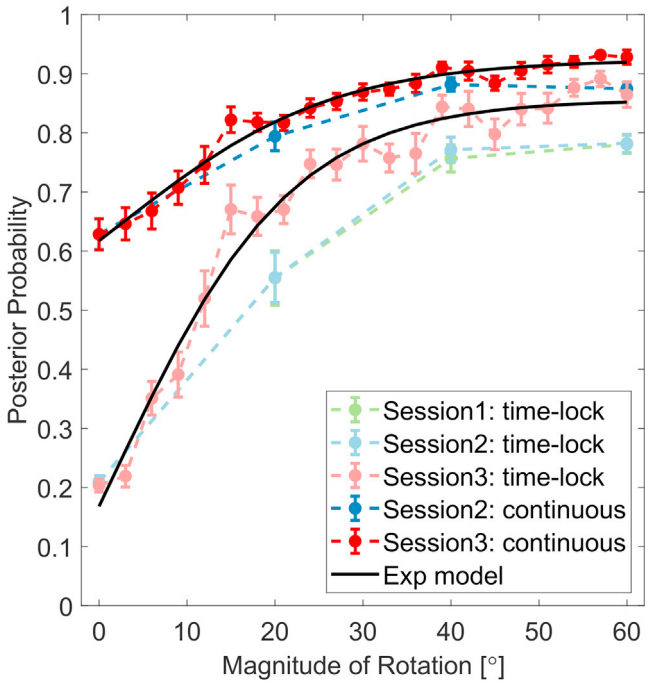

Figure 4. ErrP-BCI output over the varying magnitude of errors

Estimated posterior probabilities of each recording session for each magnitude of rotation and fitted curve for both time-lock classification and continuous decoding on the third session are presented (mean ± SE). Note that estimated posterior probability is modeled as an exponential function of the magnitude of rotation.

conscious perception of the rotation (i.e., "Yes", Figure 3C). Additionally, we revealed a significant correlation between the behavioral perceptual threshold, or inflection point, and the inferred perceptual threshold (Figure 5B). Taken together, our results suggest that ErrPs encode not only the magnitude of errors, but also the individual perceptual threshold to discern them consciously. Previous works also found a relationship between the size of the ErrP, in particular the Pe component, and the participants' confidence on the accuracy of their own response, appraised on a discrete scale.[43,44] This is a substantial difference with respect to our study where errors are not committed by subjects, but by the device they are interacting with. As recently shown,[45] the neural substrate of confidence –how humans compute the likelihood that a decision is correct, or metacognition– extends beyond the ErrP sources and, critically, metacognitive performance is better for decisions made by the subjects as compared to decisions they just observed.

Our experimental setup and findings open new avenues to probe and extend current theories of performance monitoring, which are based on response conflict tasks such as flanker (see, e.g.,[36,42] for reviews), by incorporating continuous human interaction tasks as well as analysis of the ErrP complex as a whole rather than individual peaks. Moreover, while these theories interpret that the frontocentral Pe is simply associated with fast orienting and attentional processes, our results show Pe encodes qualitatively and quantitatively more information. In particular, while we observe a larger subsequent centroparietal Pe at 400 ms (Figure S2), which has been proposed to drive adaptation,[36] the two positive deflections reflect similarly the magnitude of errors.

Our results are not limited to the theta band activity of EEG. Völker et al.[20] recently reported the presence of the high-gamma band modulation during an Erikson flanker task in both invasive and noninvasive EEG recordings. High-gamma band ([60, 90] Hz) power increased when humans performed erroneous motor actions time-locked to the Pe component of ErrPs. Consistent with their findings, our results also demonstrate that the peak high-gamma power aligns with the Pe deflection in the same high-gamma band ([60, 90] Hz, Figure 2B). Extending their results, we observed progressive increase of band power over magnitude of errors only in theta and gamma bands, but not in beta. Further, a magnitude-dependent theta-gamma phase-amplitude coupling, which has often been reported during sensory signal detection and visual perception tasks,[46,47] was also discerned (Figure 2D). Although we have further analyzed datasets collected

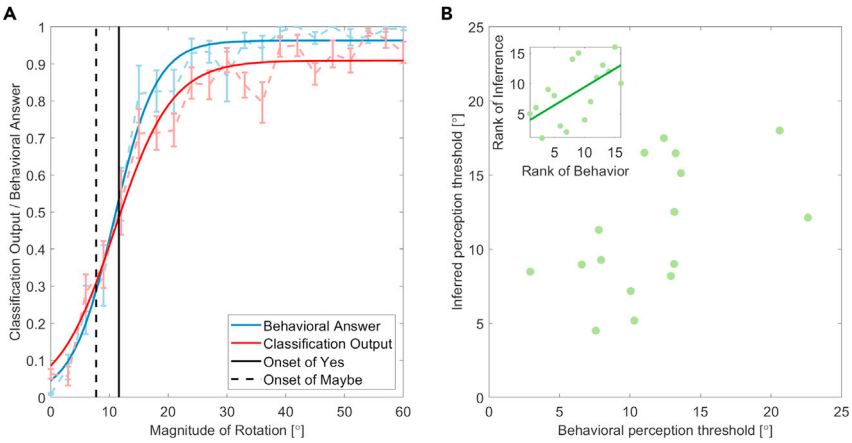

Figure 5. Inferring each subject's individual perceptual threshold to detect a visual rotation

(A) Answer to the questionnaires collected after each trial and the results of the time-locked classification on the data collected on the third session (mean ± SE). Black solid vertical line corresponds to onset of conscious perception (Yes) while black dashed line is onset of Maybe. For classification output (red), 1 means that all trials were estimated as erroneous (there was a rotation), while 0 means that all trials were estimated as correct (no rotation). For behavioral answer (blue), 1 indicates that all trials of a given rotation were consciously perceived (i.e., Yes), while 0 means that all trials were not consciously perceived (i.e., Maybe or No). Behavioral answer and classification output increased similarly over the magnitude of rotation before and after the perceptual threshold (i.e., Onset of Yes).

(B) Scatterplot of the behavioral individual perceptual threshold and the inferred perceptual threshold based on the time-locked classification of ErrPs. Each dot corresponds to one subject. Inset represents the scatterplot of ranked thresholds, and the solid line indicates the relationship between the ranked variables.

See also Figure S1B.

during our previous studies,[30,32] we did not observe such gamma band activity nor theta-gamma phase-amplitude coupling. This was neither the case for the control experiment, for both the active and the playback conditions (Figure S6). A distinction between those previous and control studies against the present study is that in the latter participants had to re-calibrate their mapping to control the cursor to complete a task. Although the active condition of the control experiment allowed participants to perform corrective actions, correct mapping was restored shortly after each error. Thus, participants did not need to adjust their mapping to complete a task. Krigolson et al.[48] showed that "correctability" of the task influences theta band activity; however, how the "correctability" modulates gamma band activity remains unclear. Increase of gamma band has been thought to represent "sharpening existing memories and formation of new motor memories"[49,50] and coupling between frequency bands would promote memory formation and neural communications.[51] Particularly in motor adaptation learning, the increased gamma band power modulation of frontal and motor brain regions has been reported during early learning, a time period in which the adaptation performance increases rapidly.[52,53] However, these reports were limited to trial-by-trial changes during adaptation learning. Our results now identified millisecond-by-millisecond theta-gamma oscillatory coupling that occurred during continuous interaction only in the case when re-calibration of a deployed strategy to control the cursor was required to accomplish the task and co-varies with magnitude of the required adjustment.

This study also uncovered a tight temporal relationship between corrective actions and the two characteristic electrophysiological deflections of ErrPs; namely, ERN and Pe. We observed ERN at 0.25 s with respect to the rotation onset (Figures 3A-3C), which corresponds to the time period where participants initiate the corrective actions to re-aim the target (Figure 1D). Similarly, Pe was observed at 0.35 s, in the middle of corrective actions. Interestingly, temporal patterns of both joystick speed and high-gamma band power were monotonically increasing, while the beta-band power was decreasing from baseline toward its peak value within the time window between ERN and Pe. Overall, our results suggest presence of rapid information transfer between theta and high-gamma band activity to activate corrective actions of right amount after detection of an error.

Initiation of a movement causes event-related desynchronization (ERD) in mu and beta rhythms.[54] In our experiment ErrPs were induced during continuous movement, and so we do not expect much interference

between ERDs and ErrPs. It has also been shown that event-related potentials like ErrPs (i.e., increase in theta power) are distinguished while subjects operate a cursor to track a moving target.[55]

Finally, our study has implications for single-trial decoding of ErrPs during continuous human-computer interactions. The individual BCI decoders exhibited good transfer across recording sessions and scalability over the varying magnitude of errors. Stable ErrP patterns over the recording sessions enabled us to deploy "Plug-and-Play" ErrP-BCIs on the second and the third session (Figure 3), in which online decoding of ErrPs were carried out since the first run of the session by transferring the decoder from the previous recordings. Transfer learning to detect ErrPs has been investigated across different error types,[56,57] cognitive workload conditions[30,58] and participants[28,59]; however, they often reported degraded classification performance. This was not the case in our experiments, where we observed consistent classification performance by transferring the personalized decoder over the different decoding sessions, especially during online continuous classification (Figures 3D and 3E; Table 2). Nevertheless, our results revealed the difficulty to detect small errors compared to large ones due to the reduced amplitude and delayed deflections of their elicited ErrPs (Figures 3A, 3B, and 4). Importantly, the latency to detect ErrPs was close to the optimal latency and very stable across sessions during online continuous decoding (Figure 3F), thus demonstrating the temporal precision of the continuous ErrP-BCI. We conjecture that such a kind of ErrP-BCI could enhance operation of assistive devices by people with severe motor disabilities. Indeed, because of their degraded residual control, these subjects will occasionally deliver wrong commands similar to the visual rotations in our experiments and will not be fast enough to execute corrective actions before the output of the ErrP-BCI will be available.

Limitations of the study

We used only 16 EEG channels to record brain oscillatory activity, which limits the analysis of ErrP sources for errors of varying magnitude. We predict, however, that neural substrates that signal ErrPs will slightly differ depending on the magnitude of errors.[60]

In the present study, errors were not internally driven, but induced by the device subjects interacted with. A previous study documented different temporal dynamics of ErrPs depending on the source of errors.[36] Although it is challenging to collect a reliable number of self-generated errors over a varying magnitude,[61] doing so will further help characterize the dynamics and neural substrates of ErrPs.

STAR★METHODS

Detailed methods are provided in the online version of this paper and include the following:

- KEY RESOURCES TABLE
- RESOURCE AVAILABILITY
  - Lead contact
  - Materials availability
  - Data and code availability
- EXPERIMENTAL MODEL AND STUDY PARTICIPANT DETAILS
  - Participants
- METHOD DETAILS
  - Experimental design
  - EEG and EOG acquisition
  - Time-frequency analysis
  - BCI decoding analysis
  - Individual perception threshold
  - Control experiment
- QUANTIFICATION AND STATISTICAL ANALYSIS
  - Behavioral analysis
  - Time-frequency analysis
  - BCI decoding performance
  - Individual perception threshold

SUPPLEMENTAL INFORMATION

Supplemental information can be found online at https://doi.org/10.1016/j.isci.2023.107524.

ACKNOWLEDGMENTS

This work was partially supported by the Hasler Foundation, Switzerland and Masason Foundation, Japan. We thank Dr. Iñaki Iturrate for helpful comments on experimental designs.

AUTHOR CONTRIBUTIONS

Conceptualization: F.I., R.C., and J.d.R.M.; Methodology: F.I., A.S., R.C., and J.d.R.M.; Formal Analysis: F.I. and J.d.R.M.; Investigation: F.I. and A.S.; Writing—original draft: F.I. and J.d.R.M.; Writing—review and editing: F.I., A.S., R.C., and J.d.R.M.

DECLARATION OF INTERESTS

The authors declare no competing interests.

INCLUSION AND DIVERSITY

We support inclusive, diverse, and equitable conduct of research.

Received: February 14, 2023
Revised: June 15, 2023
Accepted: July 28, 2023
Published: August 2, 2023

REFERENCES

1. Rabbitt, P.M. (1966). Errors and error correction in choice-response tasks. J. Exp. Psychol. *71*, 264–272. https://doi.org/10.1037/h0022853.

2. Seidler, R.D., Mulavara, A.P., Bloomberg, J.J., and Peters, B.T. (2015). Individual predictors of sensorimotor adaptability. Front. Syst. Neurosci. *9*, 100. https://doi.org/10.3389/fnsys.2015.00100.

3. Seidler, R.D., and Carson, R.G. (2017). Sensorimotor Learning: Neurocognitive Mechanisms and Individual Differences. J. NeuroEng. Rehabil. *14*, 74. https://doi.org/10.1186/s12984-017-0279-1.

4. Gehring, W.J., Goss, B., Coles, M.G.H., Meyer, D.E., and Donchin, E. (1993). A neural system for error detection and compensation. Psychol. Sci. *4*, 385–390. https://doi.org/10.1111/j.1467-9280.1993.tb00586.x.

5. Falkenstein, M., Hoormann, J., Christ, S., and Hohnsbein, J. (2000). ERP components on reaction errors and their functional significance: A tutorial. Biol. Psychol. *51*, 87–107. https://doi.org/10.1016/S0301-0511(99)00031-9.

6. Ullsperger, M., and Von Cramon, D.Y. (2001). Subprocesses of performance monitoring: A dissociation of error processing and response competition revealed by event-related fMRI and ERPs. Neuroimage *14*, 1387–1401.

7. van Schie, H.T., Mars, R.B., Coles, M.G.H., and Bekkering, H. (2004). Modulation of activity in medial frontal and motor cortices during error observation. Nat. Neurosci. *7*, 549–554.

8. Chavarriaga, R., Sobolewski, A., and Millán, J.d.R. (2014). Errare machinale est: the use of error-related potentials in brain-machine interfaces. Front. Neurosci. *8*, 208. https://doi.org/10.3389/fnins.2014.00208.

9. Spinelli, G., Tieri, G., Pavone, E.F., and Aglioti, S.M. (2018). Wronger than wrong: Graded mapping of the errors of an avatar in the performance monitoring system of the onlooker. Neuroimage *167*, 1–10.

10. Vocat, R., Pourtois, G., and Vuilleumier, P. (2011). Parametric modulation of error-related ERP components by the magnitude of visuo-motor mismatch. Neuropsychologia *49*, 360–367.

11. Hill, H. (2009). An event-related potential evoked by movement planning is modulated by performance and learning in visuomotor control. Exp. Brain Res. *195*, 519–529. https://doi.org/10.1007/s00221-009-1821-6.

12. Torrecillos, F., Albouy, P., Brochier, T., and Malfait, N. (2014). Does the processing of sensory and reward-prediction errors involve common neural resources? Evidence from a frontocentral negative potential modulated by movement execution errors. J. Neurosci. *34*, 4845–4856. https://doi.org/10.1523/JNEUROSCI.4390-13.2014.

13. Benyamini, M., Demchenko, I., and Zacksenhouse, M. (2021). Error related EEG potentials evoked by visuo-motor rotations. Brain Res. *1769*, 147606. https://doi.org/10.1016/j.brainres.2021.147606.

14. Spüler, M., and Niethammer, C. (2015). Error-related potentials during continuous feedback: Using EEG to detect errors of different type and severity. Front. Hum. Neurosci. *9*, 155. https://doi.org/10.3389/fnhum.2015.00155.

15. Chavarriaga, R., and Millán, J.d.R. (2010). Learning from EEG error-related potentials in noninvasive brain-computer interfaces. IEEE Trans. Neural Syst. Rehabil. Eng. *18*, 381–388. https://doi.org/10.1109/TNSRE.2010.2053387.

16. Brázdil, M., Roman, R., Falkenstein, M., Daniel, P., Jurák, P., and Rektor, I. (2002). Error processing–Evidence from intracerebral ERP recordings. Exp. Brain Res. *146*, 460–466.

17. Van Veen, V., and Carter, C.S. (2002). The anterior cingulate as a conflict monitor: fMRI and ERP studies. Physiol. Behav. *77*, 477–482.

18. Herrmann, M.J., Römmler, J., Ehlis, A.-C., Heidrich, A., and Fallgatter, A.J. (2004). Source localization (LORETA) of the error-related-negativity (ERN/Ne) and positivity (Pe). Brain Res. Cogn. Brain Res. *20*, 294–299.

19. Dali, G., Brosnan, M., Tiego, J., Johnson, B.P., Fornito, A., Bellgrove, M.A., and Hester, R. (2022). Examining the neural correlates of error awareness in a large fMRI study. Cerebr. Cortex *33*, 458–468. https://doi.org/10.1093/cercor/bhac077.

20. Völker, M., Fiederer, L.D.J., Berberich, S., Hammer, J., Behncke, J., Kršek, P., Tomášek, M., Marusič, P., Reinacher, P.C., Coenen, V.A., et al. (2018). The dynamics of error processing in the human brain as reflected by high-gamma activity in noninvasive and intracranial EEG. Neuroimage *173*, 564–579. https://doi.org/10.1016/j.neuroimage.2018.01.059.

21. Ferrez, P.W., and Millán, J.d.R. (2008). Error-related EEG potentials generated during simulated brain-computer interaction. IEEE Trans. Biomed. Eng. *55*, 923–929. https://doi.org/10.1109/TBME.2007.908083.

22. Ferrez, P.W., and Millán, J.d.R. (2008). Simultaneous real-time detection of motor imagery and error-related potentials for improved BCI accuracy. In International Brain-Computer Interface Workshop and Training Course, pp. 197–202.

23. Spüler, M., Bensch, M., Kleih, S., Rosenstiel, W., Bogdan, M., and Kübler, A. (2012). Online use of error-related potentials in healthy users and people with severe motor impairment increases performance of a P300-BCI. Clin. Neurophysiol. *123*, 1328–1337. https://doi.org/10.1016/j.clinph.2011.11.082.

24. Schmidt, N.M., Blankertz, B., and Treder, M.S. (2012). Online detection of error-related potentials boosts the performance of mental typewriters. BMC Neurosci. *13*, 19. https://doi.org/10.1186/1471-2202-13-19.

25. Iturrate, I., Chavarriaga, R., Montesano, L., Minguez, J., and Millán, J.d.R. (2015). Teaching brain-machine interfaces as an alternative paradigm to neuroprosthetics control. Sci. Rep. *5*, 13893. https://doi.org/10.1038/srep13893.

26. Salazar-Gomez, A.F., DelPreto, J., Gil, S., Guenther, F.H., and Rus, D. (2017). Correcting robot mistakes in real time using EEG signals. IEEE International Conference on Robotics and Automation, 6570–6577. https://doi.org/10.1109/ICRA.2017.7989777.

27. Lopes-Dias, C., Sburlea, A.I., and Müller-Putz, G.R. (2019). Online asynchronous decoding of error-related potentials during the continuous control of a robot. Sci. Rep. *9*, 17596. https://doi.org/10.1038/s41598-019-54109-x.

28. Lopes-Dias, C., Sburlea, A.I., Breitegger, K., Wyss, D., Drescher, H., Wildburger, R., and Müller-Putz, G.R. (2021). Online asynchronous detection of error-related potentials in participants with a spinal cord injury using a generic classifier. J. Neural Eng. *18*, 046022. https://doi.org/10.1088/1741-2552/abd1eb.

29. Omedes, J., Iturrate, I., Minguez, J., and Montesano, L. (2015). Analysis and asynchronous detection of gradually unfolding errors during monitoring tasks. J. Neural Eng. *12*, 056001.

30. Iwane, F., Iturrate, I., Chavarriaga, R., and Millán, J.d.R. (2021). Invariability of EEG error-related potentials during continuous feedback protocols elicited by erroneous actions at predicted or unpredicted states. J. Neural Eng. *18*, 046044. https://doi.org/10.1088/1741-2552/abfa70.

31. Iturrate, I., Grizou, J., Omedes, J., Oudeyer, P.-Y., Lopes, M., and Montesano, L. (2015). Exploiting task constraints for self-calibrated brain-machine interface control using error-related potentials. PLoS One *10*, 01314911–e131515. https://doi.org/10.1371/journal.pone.0131491.

32. Batzianoulis, I., Iwane, F., Wei, S., Correia, C.G.P.R., Chavarriaga, R., Millán, J.d.R., and Billard, A. (2021). Customizing skills for assistive robotic manipulators, an inverse reinforcement learning approach with error-related potentials. Commun. Biol. *4*, 1406–1414. https://doi.org/10.1038/s42003-021-02891-8.

33. Silversmith, D.B., Abiri, R., Hardy, N.F., Natraj, N., Tu-Chan, A., Chang, E.F., and Ganguly, K. (2021). Plug-and-play control of a brain-computer interface through neural map stabilization. Nat. Biotechnol. *39*, 326–335.

34. Jahani, A., Schwey, A., Bernier, P.-M., and Malfait, N. (2020). Spatially distinct beta-band activities reflect implicit sensorimotor adaptation and explicit re-aiming strategy. J. Neurosci. *40*, 2498–2509. https://doi.org/10.1523/JNEUROSCI.1862-19.2020.

35. Alayrangues, J., Torrecillos, F., Jahani, A., and Malfait, N. (2019). Error-related modulations of the sensorimotor post-movement and foreperiod beta-band activities arise from distinct neural substrates and do not reflect efferent signal processing. Neuroimage *184*, 10–24. https://doi.org/10.1016/j.neuroimage.2018.09.013.

36. Ullsperger, M., Fischer, A.G., Nigbur, R., and Endrass, T. (2014). Neural mechanisms and temporal dynamics of performance monitoring. Trends Cognit. Sci. *18*, 259–267.

37. Lopes-Dias, C., Sburlea, A.I., and Müller-Putz, G.R. (2018). Masked and unmasked error-related potentials during continuous control and feedback. J. Neural Eng. *15*, 036031. https://doi.org/10.1088/1741-2552/aab806.

38. Cunningham, H.A. (1989). Aiming error under transformed spatial mappings suggests a structure for visual-motor maps. J. Exp. Psychol. Hum. Percept. Perform. *15*, 493–506.

39. Hinder, M.R., Tresilian, J.R., Riek, S., and Carson, R.G. (2008). The contribution of visual feedback to visuomotor adaptation: How much and when? Brain Res. *1197*, 123–134.

40. Hinder, M.R., Riek, S., Tresilian, J.R., de Rugy, A., and Carson, R.G. (2010). Real-time error detection but not error correction drives automatic visuomotor adaptation. Exp. Brain Res. *201*, 191–207. https://doi.org/10.1007/s00221-009-2025-9.

41. Iwane, F., Chavarriaga, R., Iturrate, I., and Millán, J.d.R. (2016). Spatial filters yield stable features for error-related potentials across conditions. IEEE Int. Conf. Syst. Man Cybern. 661–666.

42. Ullsperger, M., Danielmeier, C., and Jocham, G. (2014). Neurophysiology of performance monitoring and adaptive behavior. Physiol. Rev. *94*, 35–79.

43. Scheffers, M.K., and Coles, M.G.H. (2000). Performance monitoring in a confusing world: Error-related brain activity, judgments of response accuracy, and types of errors. J. Exp. Psychol. Hum. Percept. Perform. *26*, 141–151.

44. Boldt, A., and Yeung, N. (2015). Shared neural markers of decision confidence and error detection. J. Neurosci. *35*, 3478–3484. https://doi.org/10.1523/JNEUROSCI.0797-14.2015.

45. Pereira, M., Faivre, N., Iturrate, I., Wirthlin, M., Serafini, L., Martin, S., Desvachez, A., Blanke, O., Van De Ville, D., and Millán, J.d.R. (2020). Disentangling the origins of confidence in speeded perceptual judgments through multimodal imaging. Proc. Natl. Acad. Sci. USA *117*, 8382–8390.

46. Schroeder, C.E., and Lakatos, P. (2009). Low-frequency neuronal oscillations as instruments of sensory selection. Trends Neurosci. *32*, 9–18. https://doi.org/10.1016/j.tins.2008.09.012.

47. Händel, B., and Haarmeier, T. (2009). Cross-frequency coupling of brain oscillations indicates the success in visual motion discrimination. Neuroimage *45*, 1040–1046. https://doi.org/10.1016/j.neuroimage.2008.12.013.

48. Krigolson, O.E., Holroyd, C.B., Van Gyn, G., and Heath, M. (2008). Electroencephalographic correlates of target and outcome errors. Exp. Brain Res. *190*, 401–411. https://doi.org/10.1007/s00221-008-1482-x.

49. Herrmann, C.S., Fründ, I., and Lenz, D. (2010). Human gamma-band activity: A review on cognitive and behavioral correlates and network models. Neurosci. Biobehav. Rev. *34*, 981–992. https://doi.org/10.1016/j.neubiorev.2009.09.001.

50. Sauseng, P., Griesmayr, B., Freunberger, R., and Klimesch, W. (2010). Control mechanisms in working memory: A possible function of EEG theta oscillations. Neurosci. Biobehav. Rev. *34*, 1015–1022. https://doi.org/10.1016/j.neubiorev.2009.12.006.

51. Lisman, J. (2010). Working Memory: The importance of theta and gamma oscillations. Curr. Biol. *20*, R490–R492. https://doi.org/10.1016/j.cub.2010.04.011.

52. Perfetti, B., Moisello, C., Landsness, E.C., Kvint, S., Lanzafame, S., Onofrj, M., Di Rocco, A., Tononi, G., and Ghilardi, M.F. (2011). Modulation of gamma and theta spectral amplitude and phase synchronization is associated with the development of visuo-motor learning. J. Neurosci. *31*, 14810–14819. https://doi.org/10.1523/JNEUROSCI.1319-11.2011.

53. Struber, L., Baumont, M., Barraud, P.-A., Nougier, V., and Cignetti, F. (2021). Brain oscillatory correlates of visuomotor adaptive learning. Neuroimage *245*, 118645. https://doi.org/10.1016/j.neuroimage.2021.118645.

54. Pfurtscheller, G., and Lopes da Silva, F.H. (1999). Event-related EEG/MEG synchronization and desynchronization: Basic principles. Clin. Neurophysiol. *110*, 1842–1857.

55. Pereira, M., Sobolewski, A., and Millán, J.d.R. (2017). Action monitoring cortical activity coupled to submovements. eNeuro *4*. https://doi.org/10.1523/ENEURO.0241-17.2017.

56. Kim, S.K., and Kirchner, E.A. (2013). Classifier transferability in the detection of error related potentials from observation to interaction. IEEE Int. Conf. Syst. Man Cybern. 3360–3365. https://doi.org/10.1109/SMC.2013.573.

57. Ehrlich, S.K., and Cheng, G. (2019). A Feasibility study for validating robot actions using EEG-based error-related potentials. Int. J. Soc. Robot. *11*, 271–283. https://doi.org/10.1007/s12369-018-0501-8.

58. Iturrate, I., Chavarriaga, R., Montesano, L., Minguez, J., and Millán, J.d.R. (2014). Latency correction of event-related potentials

between different experimental protocols. J. Neural Eng. *11*, 036005.

59. Lopes-Dias, C., Sburlea, A.I., and Müller-Putz, G.R. (2020). A generic error-related potential classifier offers a comparable performance to a personalized classifier. In Int. Conf. IEEE Eng. Med. Biol. Soc., pp. 2995–2998. https://doi.org/10.1109/EMBC44109.2020.9176640.

60. Smith, B.W., Mitchell, D.G.V., Hardin, M.G., Jazbec, S., Fridberg, D., Blair, R.J.R., and Ernst, M. (2009). Neural substrates of reward magnitude, probability, and risk during a wheel of fortune decision-making task. Neuroimage *44*, 600–609. https://doi.org/10.1016/j.neuroimage.2008.08.016.

61. Iwane, F., Dash, D., Salamanca-Giron, R.F., Hayward, W., Bönstrup, M., Buch, E.R., and Cohen, L.G. (2023). Combined low-frequency brain oscillatory activity and behavior predict future errors in human motor skill. Curr. Biol. https://doi.org/10.1016/j.cub.2023.06.040.

62. Schlögl, A., Keinrath, C., Zimmermann, D., Scherer, R., Leeb, R., and Pfurtscheller, G. (2007). A fully automated correction method of EOG artifacts in EEG recordings. Clin. Neurophysiol. *118*, 98–104. https://doi.org/10.1016/j.clinph.2006.09.003.

63. Daubechies, I. (1990). The wavelet transform, time-frequency localization and signal analysis. IEEE Trans. Inf. Theor. *36*, 961–1005. https://doi.org/10.1109/18.57199.

64. Delorme, A., and Makeig, S. (2004). EEGLAB: An open source toolbox for analysis of single-trial EEG dynamics including independent component analysis. J. Neurosci. Methods *134*, 9–21. https://doi.org/10.1016/j.jneumeth.2003.10.009.

65. Grandchamp, R., and Delorme, A. (2011). Single-trial normalization for event-related spectral decomposition reduces sensitivity to noisy trials. Front. Psychol. *2*, 236. https://doi.org/10.3389/fpsyg.2011.00236.

66. Iwane, F., Lisi, G., and Morimoto, J. (2019). EEG Sensorimotor correlates of speed during forearm passive movements. IEEE Trans. Neural Syst. Rehabil. Eng. *27*, 1667–1675. https://doi.org/10.1109/TNSRE.2019.2934231.

67. Hülsemann, M.J., Naumann, E., and Rasch, B. (2019). Quantification of phase-amplitude coupling in neuronal oscillations: Comparison of phase-locking value, mean vector length, modulation index, and generalized-linear-modeling-cross-frequency-coupling. Front. Neurosci. *13*, 573. https://doi.org/10.3389/fnins.2019.00573.

68. Spüler, M., Walter, A., Rosenstiel, W., and Bogdan, M. (2014). Spatial filtering based on canonical correlation analysis for classification of evoked or event-related potentials in EEG data. IEEE Trans. Neural Syst. Rehabil. Eng. *22*, 1097–1103. https://doi.org/10.1109/TNSRE.2013.2290870.

69. Spüler, M. (2017). Spatial filtering of EEG as a regression problem. In Graz Brain-Computer Interface Conference. https://doi.org/10.3217/978-3-85125-533-1-84.

70. Congedo, M., Barachant, A., and Bhatia, R. (2017). Riemannian geometry for EEG-based brain-computer interfaces; a primer and a review. Brain-Computer Interfaces *4*, 155–174.

71. Barachant, A., Bonnet, S., Congedo, M., and Jutten, C. (2012). Multiclass brain–computer interface classification by Riemannian geometry. IEEE Trans. Biomed. Eng. *59*, 920–928.

72. Treutwein, B., and Strasburger, H. (1999). Fitting the psychometric function. Percept. Psychophys. *61*, 87–106. https://doi.org/10.3758/BF03211951.

73. Klein, S.A. (2001). Measuring, estimating, and understanding the psychometric function: A commentary. Percept. Psychophys. *63*, 1421–1455. https://doi.org/10.3758/BF03194552.

74. García-Pérez, M.A., Alcalá-Quintana, R., Woods, R.L., and Peli, E. (2011). Psychometric functions for detection and discrimination with and without flankers. Atten. Percept. Psychophys. *73*, 829–853. https://doi.org/10.3758/s13414-010-0080-8.

75. David, F.N. (1938). Tables of the Ordinates and Probability Integral of the Distribution of the Correlation Coefficient in Small Samples (Cambridge University Press).

76. Bonett, D.G., and Wright, T.A. (2000). Sample size requirements for estimating Pearson, Kendall and Spearman correlations. Psychometrika *65*, 23–28. https://doi.org/10.1007/BF02294183.

STAR★METHODS

KEY RESOURCES TABLE

REAGENT or RESOURCE	SOURCE	IDENTIFIER
Deposited data		
Behavior and EEG data	This paper	Zenodo: https://doi.org/10.5281/zenodo.6415455
Software and algorithms		
MATLAB 2018b	The Mathworks, Natick, MA, USA	https://www.mathworks.com/products/matlab.html
BioSig Toolbox	The BioSig project	http://biosig.sourceforge.net
EEGLAB	Delorme and Makeig[64]	https://sccn.ucsd.edu/eeglab/index.php
Covariance Toolbox	Barachant et al.[71]	GitHub: https://github.com/alexandrebarachant/covariancetoolbox
Analyzing Neural Time Series	Mike X Cohen	https://doi.org/10.7551/mitpress/9609.001.0001
Custom software code	This paper	Zenodo: https://doi.org/10.5281/zenodo.6415455
Other		
g.USBAMP RESEARCH	g.tec medical engineering, Austria	https://www.gtec.at/product/gusbamp-research/
ActiveTwo System	BioSemi B.V., Amsterdam, the Netherlands	https://www.biosemi.com/index.htm
Dualshock 4 wireless controller	Sony Interactive Entertainment, Japan	https://www.playstation.com/en-us/accessories/dualshock-4-wireless-controller/

RESOURCE AVAILABILITY

Lead contact

Further information and requests for resources should be directed to and will be fulfilled by the Lead contact, José del R. Millán (jose.millan@austin.utexas.edu).

Materials availability

This study did not generate new materials.

Data and code availability

- De-identified data, permanently unlinked from all personal identifiable information (PII), were used in the present study. These data is available at Zenodo: https://doi.org/10.5281/zenodo.6415455.
- All original code has been deposited at Zenodo and is publicly available as of the date of publication. DOIs are listed in the key resources table.
- Any additional information required to reanalyze the data reported in this paper is available from the lead contact upon request.

EXPERIMENTAL MODEL AND STUDY PARTICIPANT DETAILS

Participants

Sixteen able-bodied healthy subjects (four females, 23 ± 1 years old) participated in the experiment, which consisted of three recording sessions (days). The experimental protocol was approved by the local ethics commission (PB_2017-00295). Written informed consent was collected from all participants before conducting the experiment. During the experiment, participants sat on a comfortable chair in front of a laptop with a 14-inch display that visualized the experimental protocol.

METHOD DETAILS

Experimental design

The graphical interface of the experiment was displayed on a laptop. Each trial started after a button press of a game-pad (DualShock4, Sony, Japan). A blue circle represented the cursor, which was controlled by the left joystick of the game-pad, and a red square represented the goal location. Participants were instructed to bring the cursor to the target as quickly as possible without performing gross movement nor excessive eye blinks. The speed of the cursor was kept constant (750 pixel/s) during the cursor reaching task as long as the joystick was pressed. Time duration of a trial and cumulative average duration of trials within a run were displayed after each trial. Averaged duration of a trial was 3.5 $\pm$ 0.2 s. A trial was considered complete when the cursor reached the goal.

The goal location was randomly chosen for each trial among six potential locations; i.e., top-left, middle-left, low-left, top-right, middle-right and low-right. Initial position of the cursor was at the other side of the target at a random height to ensure enough distance (at least 1960 pixel) between the initial position of the cursor and the goal. For example, if the goal was on the right side, the cursor was placed on the left side at a random height and vice versa. In 30% of trials, the joystick-to-cursor mapping was rotated when the cursor exceeded a pre-defined invisible boundary. The boundary was randomly determined for each trial. The rotation persisted until the end of the trial, thus participants had to perform corrective action to complete a trial. Trials with a visual rotation were defined as ''erroneous trials'', and others as ''correct trials''. The magnitude of rotation was fixed to 20°, 40° and 60° on the first and the second sessions. On the third session, the magnitude of rotation was between 3° to 60° with a step of 3°, and after each trial participants were asked whether they perceived the rotation, maybe or not (''Yes'', ''Maybe'' or ''No'').

Participants performed 10 runs of 40 trials in each session (400 × 3 trials in total). Before these runs, participants performed 20 trials where they got accustomed to the task and made eye movements for 90 s for estimating regression parameters to remove EOG artifacts from their EEG during the actual experiment.[62]

Participants executed the experiment without receiving online feedback on the first session. We provided subjects with online feedback on the second and the third sessions by changing the color of the cursor upon ErrP detection. On the second session, presence of ErrPs was continuously monitored during cursor control, and the decoder was re-calibrated after each run. On the third session, we carried out continuous decoding of ErrPs without re-calibrating the decoder, which was built with data from the first and the second sessions, except for the parameters to remove EOG artifact.

EEG and EOG acquisition

16 EEG and 3 EOG electrodes were recorded at 512 Hz throughout the experiment (two synchronized g.USBAmp, g.tec medical engineering, Austria). Active EEG electrodes were located at Fz, FC3, FC1, FCz, FC2, FC4, C3, C1, Cz, C2, C4, CP3, CP1, CPz, CP2 and CP4 in 10/10 international coordinates, and EOG electrodes were placed at above the nasion and below the outer canthi of the eyes. The ground electrode was placed on the forehead (AFz) and the reference electrode was placed on the left earlobe. We used the same reference and ground electrode for both EEG and EOG signals. EEG and EOG signals were notch filtered at 50 Hz by the amplifiers. To reduce signal contamination, participants were asked to avoid excessive eye movements and blinks during trials.

Time-frequency analysis

To characterize the time-frequency representation of ErrPs elicited by visual rotations, we computed a Morlet's wavelet time-frequency decomposition.[63] After applying a 2nd order non-causal high-pass Butterworth filter with the cut-off frequency of 1 Hz and current source density (CSD), EEG signals were epoched in the time window [-0.2, 1.0] s with respect to the onset of rotations. For each single-trial EEG epoch we performed the Morlet Wavelet time-frequency decomposition[64] in the frequency range [3, 100] Hz, resulting in a wavelet coefficient matrix with 126 time points and 97 log-spaced frequency bins. Each of time windows were composed of 427 samples (0.83 s) overlapped by 51 samples (0.1 s); while the number of cycles ranges from 3 to 20 at highest. The resulting coefficients were used to extract spectral power and phase-amplitude coupling.

To compute the spectral power induced by visual rotations, we used the event-related spectral perturbation (ERSP) approach.[65] This approach is less sensitive to noisy trials than classical baseline correction methods and produces a non-skewed power distribution. In detail, separately for each subject and experimental condition, we apply a single-trial full-epoch baseline correction, before averaging across trials and removing the trial-averaged pre-stimulus (i.e., from -0.25 to 0.0 s) baseline. Baselines were corrected using the gain model assumption (i.e., divide by the baseline) instead of the additive model (i.e., subtract the baseline).[65,66] Finally, the trial-averaged pre-stimulus corrected time frequency coefficients were log-transformed (10 log_{10}).

To compute the phase-amplitude coupling, we first identified the latency of ERN and Pe (0.25 and 0.35 s, respectively), then used the mean vector length (MVL) method.[67] This method estimates the coupling between phase frequency f_p and amplitude frequency f_a from a number of epochs N, by mapping phase time series $\varphi_{f_p}(t,n)$ and amplitude time series $A_{f_a}(t,n)$ to a complex-values vector at each time point, t, and each epoch, n. To quantify the coupling between f_p and f_a, the MVL method measures the length of the average vector and computes phase-amplitude coupling as follows:

$$MVL(f_a,f_p) = \left| \frac{1}{N} \sum_{n=1}^{N} A_{f_a}(t,n) e^{j\varphi_{f_p}(t,n)} \right|$$

BCI decoding analysis

EEG signals were band-pass filtered with a 4th order causal Butterworth filter with cutoff frequencies of [1, 10] Hz, for both online and offline analyses. To build the individual decoders, ErrPs were segmented into epochs in the time window of [0.2, 0.8] s with respect to the onset of the visual rotation. Firstly, to enhance the signal-to-noise ratio of the EEG, we applied a spatial filter based on canonical correlation analysis (CCA).[41,68] This spatial filter method transforms the averaged ErrPs to a subspace containing different ERP components.[69] Only the first three components were kept for the subsequent analysis. This number was determined based on the data collected on the first session by performing pseudo-continuous decoding in cross validation.

For every trial, we extracted three complementary types of features: the decimated signal amplitude per CCA component at 64 Hz; power spectral densities per CCA component from 4 to 10 Hz with a step of 2 Hz; and the covariance matrix on Riemannian geometry, which computes a low-dimensionality manifold representation from a non-linear combination of the EEG component space.[70] In order to include information of the EEG temporal dynamics in the Riemannian spatial covariance matrix, the epoch X was augmented with an individual template T representing the grand average of erroneous trials in the training set:

$$Z = [X \quad T]$$

$$C_z = \frac{1}{s} Z^T Z = \frac{1}{s} \begin{pmatrix} X^T X & X^T T \\ T^T X & T^T T \end{pmatrix}$$

where s denotes number of time samples of an epoch.

The covariance between X and T allows to capture the temporal dynamics of multi-component EEG signals with respect to the template. The covariance matrix was then projected on the tangent space, computed only on the training dataset.[71] All computed features were concatenated and normalized within the range of [0, 1]. From this feature vector x, we computed the estimated posterior probability of having detected an error, $p(error|x)$ using diagonal linear discriminant analysis (LDA). The decoding outputs were then scaled within the range of [0, 1] based on the following logistic function:

$$p(error|\mathbf{x}) = \frac{1}{1+e^{-(\mathbf{w}'\mathbf{x}+b)}}.$$

In order to continuously monitor the presence or absence of ErrPs, we analyzed the EEG signal with a sliding window, online or offline.[27,30]

To compute the estimated posterior probability of the training data without overfitting, aforementioned signal processing was performed in a leave-one-run-out cross-validation manner. Training folds were

used to create an ErrP decoder, while the testing fold was used to compute the continuous modulation of posterior probability during cursor control with a sliding window at 32 Hz, 16-sample shift. In order to infer participants' erroneous perception in a continuous manner and provide them with the feedback upon the detection of ErrPs, two hyperparameters were optimized besides the ErrP decoder; namely, smoothing factor and decision threshold. The smoothing factor indicates length of the time window for an online moving average filter on the estimated posterior probabilities, ranging from 1 to 16 with a step of 1. The decision threshold determined presence or absence of erroneous perception, ranging from 0 to 1 with a step of 0.01. Hyperparameter optimization was carried out in a grid search manner. Specifically, we computed the Matthew's correlation coefficient (MCC) for each pair of hyperparameters based on a confusion matrix. With a pair of hyperparameters, a correct trial was properly classified if the smoothed posterior probability did not exceed the decision threshold (True Negative). If the smoothed posterior probability in a correct trial exceeded the decision threshold, the trial was considered as erroneous (False Positive). On the other hand, an erroneous trial was correctly classified if the posterior probability exceeded the decision threshold in a time window of [0.5, 1.1] s with respect to the onset of the rotation (True Positive). This time window of [0.5, 1.1] s was determined as the optimal latency was 0.8 s and we allowed 0.3 s of temporal difference with respect to the optimal latency. If the averaged posterior probability in an erroneous trial exceeded the decision threshold outside the aforementioned time window or did not exceed the decision threshold, it was considered as wrong classification (False Negative). For each pair of hyperparameters we computed their MCC, a 16 × 101 matrix for each testing fold. The pair of hyperparameters with the highest MCC, averaged over the testing folds, was chosen as the optimal. Once the pair of optimal hyperparameters was determined, we used all the available data to re-compute the ErrP decoder to be deployed subsequently for online continuous decoding. Decoder re-calibrations during the second session —from runs 2 to 10— used all available data up to that moment (i.e., first session plus previous runs in second session), and re-estimated the pair of optimal hyperparameters. On the third session, the ErrP decoder was calibrated by using all data of the first and second session (800 trials in total) and EOG calibration data recorded at the beginning of the third session. On the second and the third sessions, we provided participants with the online feedback when the smoothed posterior probability exceeded the decision threshold for the first time in a trial.

Individual perception threshold

In order to model behavioral perception and ErrP decoding output over the magnitudes of rotation (Figures 4 and 5), we used the following exponential rule, which has been used to model participants' binary behavioral responses[72,73]:

$$y = k_1 + \frac{k_2}{1+e^{-k_3(x-k_4)}}$$

where $k_{1\text{-}4}$ represents the minimum value, maximum value, magnitude of slope and inflection point of the curve, respectively; and x represents the magnitude of rotation. Parameters $k_{1\text{-}4}$ were estimated by gradient descent with the objective function defined as the root mean square error between the observation and the fitted model. k_1 was fixed to 0 when modelling the behavioral answer and the classification output.[73,74] The inflection point of the corresponding fitted curve (k_4) was used as the behavioral or inferred perception thresholds.

Control experiment

Twelve subjects (25-40 years of age, all males and right-handed) participated in the control experiment (Figure S4). It consisted of two sessions aiming to confirm the impact of corrective actions on the observed relationship between the visual rotation magnitude and the ErrP amplitude as well as on the gamma band activity. In the first session, subjects used a standard PC mouse with their right hand to move the cursor and click on the goal (*active* condition). Upon the cursor reaching the goal and the subject pressing the left mouse button, the goal dimmed with an audible click. If the subject kept the cursor stationary on the goal for 1 s, another icon lit up at a location 60 mm up, down, left or right of the current location, forming a square. The experiment ended after the correct completion of 500 trials. In about 30% of trials, the mouse-to-cursor mapping was rotated by 20°, 40° or 60° for either 300 or 500 ms relative to movement onset. After this brief perturbation period, the normal mapping was reinstated, allowing subjects to complete the movement. Thus, participants did not compensate the rotation of mapping, but required corrective motor actions to complete a trial. During the second session, participants monitored their replayed cursor movements from the first experiment and were asked to report any observed perturbation after each trial (*playback* condition). We fixed the resting period preceding each movement to 2 s to eliminate

the element of surprise. A 64-channel EEG was acquired at the sampling frequency of 2048 Hz with a 24-bit resolution using active electrodes in an extended 10-20 setup (ActiveTwo system, BioSemi B.V., Amsterdam, the Netherlands). We implemented the same time-frequency analysis and computed grand-averaged EEG error-related activity relative to the onset of cursor movement.

QUANTIFICATION AND STATISTICAL ANALYSIS

Behavioral analysis

Pearson's correlation analysis was performed to test progression of run-wise mean reaction time over the three experimental sessions.

Time-frequency analysis

Paired Wilcoxon signed-rank tests were used to compare baseline-corrected ERSP between correct and erroneous trials. Time and frequency windows were visually identified for each frequency band. Subsequently, Spearman's correlation analyses were performed to test progression of ERSP over the magnitude of errors.

BCI decoding performance

The time-locked and the continuous decoding performance were tested for significance using paired Wilcoxon signed-rank test. Pearson's correlation analyses were used to test progression of run-wise decoding performance for the second and the third session.

Individual perception threshold

Spearman's correlation analysis and Wilcoxon's signed rank test were used to evaluate if the inferred perception threshold or the levels of engagement covaried with the behavioral one while having comparable median values. We used these non-parametric approaches because of the small sample size (N=16)[75,76] and to reduce contamination by outliers.